

Influence of Microstructure on Residual Thermal Stresses in $\text{TiC}_x\text{N}_{1-x}$ and $\alpha\text{-Al}_2\text{O}_3$ Coatings on WC-Co Tool Inserts

H. Chien*, Z. Ban**, P. Prichard**, Y. Liu** and G.S. Rohrer*

*Department of Materials Science and Engineering, Carnegie Mellon University, Pittsburgh, PA, 15213

** Kennametal Incorporated, 1600 Technology way, P.O. Box 231, Latrobe, PA 15650

Abstract

The microstructures of chemical vapor deposited coatings on four tool inserts have been comprehensively characterized using electron backscatter diffraction mapping and these data have been used as input for finite element models used to calculate the residual thermal strains in the coatings. The results indicate that the thermal strains and stored elastic energy in the $\alpha\text{-Al}_2\text{O}_3$ layer are larger than in the $\text{TiC}_x\text{N}_{1-x}$ layer. Furthermore, the mean value and distribution of stored elastic energy are influenced by the texture in the alumina layer. Coatings with weaker texture have a broader distribution of thermal stresses. Coatings with alumina oriented so that the [0001] direction is parallel to the film growth direction have less stored elastic energy. This is because the thermal expansion perpendicular to [0001] is less than the thermal expansion parallel to [0001] and, therefore, the thermal expansion mismatch between the alumina coating and the substrate is minimized when grains are oriented with [0001] perpendicular to the substrate.

Keywords

Coatings, Microstructure, Texture, Hardness, Thermal Stresses, Finite Element Model

Introduction

Multilayer coatings are often used to enhance the performance, durability, and wear resistance of cemented carbide cutting tool inserts. In the present paper, we focus on $\text{TiC}_x\text{N}_{1-x}||\alpha\text{-Al}_2\text{O}_3||\text{TiN}$ coatings deposited by chemical vapor deposition (CVD) on WC/Co substrates. In these coatings, the $\text{TiC}_x\text{N}_{1-x}$ ($0.3 < x < 0.5$) and $\alpha\text{-Al}_2\text{O}_3$ layers are each less than 10 μm thick and the TiN-capping layer is approximately 1 μm thick. The coatings considered here are representative of the coatings commonly used in the US and Western Europe. These coatings have microstructures that consist of columnar grains with diameters in the range of 0.5 to 1.0 microns [1]. The WC/Co substrates are generally untextured, the $\text{TiC}_x\text{N}_{1-x}$ layer usually has weak (112) texture and is highly twinned, and the alumina layer can be prepared with a variety of textures including (0001), $(10\bar{1}2)$, $(10\bar{1}4)$, and $(10\bar{1}0)$ [2-5].

Because these coatings are deposited at temperatures 600 to 800 °C above room temperature, residual thermal stresses develop upon cooling. There are two sources of these stresses. One source is the mismatch between the thermal expansion of the substrate and coatings. Because the substrate is so much thicker than the coatings, the coatings are constrained to change shape with the substrate. For the coatings of interest in this paper, the coefficient of thermal expansion of the substrate is smaller than that of the coatings, so at room temperature, the coatings are loaded in tension. Considering the relative

values of the thermal expansion coefficients and modulus of the coating, the expected (unrelaxed) stresses arising from thermal expansion mismatch are on the order of 2 to 3 GPa. The second source of residual thermal stress is the anisotropic thermal expansion of α -Al₂O₃. The linear coefficient of thermal expansion (CTE) along the *a*-axis is smaller than along the *c*-axis [6]. Therefore, if there is any misalignment between adjacent grains, incompatible shape changes during cooling lead to residual stresses. We will refer to these stresses as misorientation stresses. Measurements have shown that the average value of the misorientation stress in an α -Al₂O₃ polycrystal with a 2 micron grain size is on the order of 100 MPa [6]. Finite element calculations have shown that there is a wide distribution of stresses that can reach as high as 500 MPa and that these stresses are sensitive to texture [7].

Because the stress applied by the substrate exceeds the fracture strength of the coating, vertical cracks are formed in the coating that partially relieve the stress. In textured coatings, these cracks have an average spacing in the range of 40 to 80 microns [4]. Note that while the cracks are capable of partially relaxing the long range strains that arise from the substrate, they are less effective in relaxing the more local grain-to-grain misorientation strains. The residual stresses in textured coatings have been measured to be in the range of 400 to 700 MPa [5]. Therefore, in the partially relaxed coating, the misorientation stresses can make up a significant fraction of the complete residual stress.

Texture in the alumina layer can influence the thermal stresses in two ways. First, because the CTE along the *c* and *a* axes is different, alignment of the axis with the smaller CTE (the *a*-axis) parallel to the substrate plane should reduce the strain needed to make the coating conform to the substrate. The second effect of texture is to reduce the misorientation stresses. The more well aligned the *c*-axes are, the lower the misorientation stresses [7]. Therefore, basal oriented growth should reduce tensile strain arising from both the substrate effect and from local misorientations. The main objective of the work described here is to test this idea.

Because of its effect on thermal stresses and the microcracking, the texture in the alumina layer is also thought to influence the mechanical integrity and performance of the coating. Texture might also influence the mechanical properties of the coating because of alumina's anisotropic thermoelastic properties and anisotropic of the plastic response. For the cutting of ferritic-pearlitic steels with 0.45 w/o C, alumina with $\langle 10\bar{1}4 \rangle$ texture has been reported to have superior properties. [2] For the cutting of tempered steel or cast iron, (0001) texture has been reported to have superior properties. Therefore, the ideal texture may be dependent on the particular application [4].

In the current paper, the thermal stresses in tool insert coatings with different microstructures are calculated. The microstructures of four different coatings were characterized by electron backscatter diffraction (EBSD) mapping. The object oriented finite element analysis program (OOF) [8] was then used to translate the microstructural data into a mesh that can be used to simulate the thermal stresses that develop upon cooling.

Methods

We compare the microstructures of four tool inserts. Three of the four have already been described in reference [5] where they were referred to as samples 1, 2, and 4. The same designations are used here. The procedures for acquiring the microstructure data and determining the grain sizes of the new sample (labeled 3) were essentially the same as the procedures used for the first three samples. One difference is that the new electron backscatter diffraction (EBSD) data was acquired on a different scanning electron microscope. The FEI Quanta 200 FE ESEM allows low vacuum operation and this reduces charging. Therefore, the new sample was examined without the conductive coating that was used in the previous work. The EBSD data was recorded with a 1.0 micron step size for the alumina layer and a 0.5 micron step size for the Ti_xN_{1-x} and substrate.

The EBSD maps were prepared by cropping the poorly resolved regions and then applying a grain dilation clean-up using the TSL-OIM software. The purpose of the clean-up procedure is to remove

unindexed or incorrectly indexed points. In this process, the minimum misorientation distinguishing separate grains was 5° and the minimum number of pixels per grain was 5. The final step was to assign a single orientation to all of the pixels within a grain.

To construct the models, representative EBSD maps, approximately 40 microns wide, of the $\text{TiC}_x\text{N}_{1-x}$ layer and the $\alpha\text{-Al}_2\text{O}_3$ layer were joined together as illustrated in Fig. 1. Our model imposes an abrupt interface between the different layers of the coating. In reality, there are interfacial regions with a very fine grain size. However, the structures of these interfacial regions are beyond the resolution of EBSD. Because our structural description of the interface is not realistic, we will not interpret information from these regions.

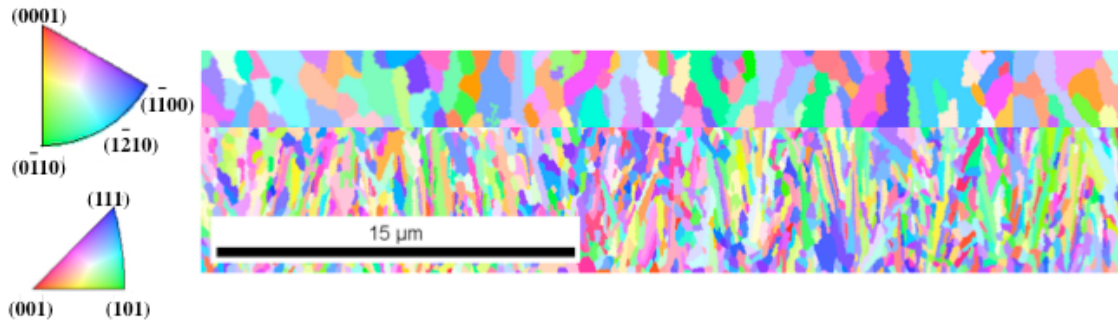


Fig. 1: Inverse pole figure maps for the $\alpha\text{-Al}_2\text{O}_3$ (upper) and $\text{TiC}_x\text{N}_{1-x}$ (lower) and layers of sample 3. Different colors indicate different grain orientations, according to the legends on the left.

The OOF2 software package (OOF2, version 2.0.4, National Institute of Standards and Technology, Gaithersburg, MD) was used to create meshes from the EBSD maps and calculate the responses of the discretized microstructures to thermal and mechanical loads. The calculation used the crystal orientation data and the anisotropic thermoelastic properties of the material. Two different calculations were performed: those to evaluate the misorientation related stresses in the alumina alone and those to evaluate the combined effects of the misorientation related stress and the substrate related stress. In both cases, the properties in Table I were assigned to the corresponding phase in the model. The domain of the computation included more 10,000 finite elements.

Table I: Physical Properties of the Materials used for the Simulations

Material	Young's Modulus (GPa)	Poisson's ratio	Coefficient of Thermal Expansion ($\times 10^6, \text{K}^{-1}$)	Elastic Constants (GPa)
TiN	-	-	9.35 ^a	$C_{11} = 625$ $C_{12} = 165$ $C_{44} = 163$ $A=0.709^b$
TiC	-	-	7.4 ^c	$C_{11} = 513$ $C_{12} = 106$ $C_{44} = 178$ $A=0.875^d$
Al_2O_3	-	-	$\alpha_{11} = 7.67$ $\alpha_{33} = 8.52^e$	$C_{11} = 497$ $C_{12} = 163$ $C_{13} = 116$ $C_{14} = 22$ $C_{33} = 501$ $C_{44} = 147^f$
WC	-	-	$\alpha_{11} = 5.2$ $\alpha_{33} = 7.3^g$	$C_{11} = 720$ $C_{12} = 254$ $C_{13} = 267$ $C_{33} = 972$ $C_{44} = 328^g$
Co	211 ^g	0.31 ^g	14.0 ^g	-

(a) ref. [10], (b) ref. [11] (c) ref. [12] (d) ref. [13] (e) ref [14] at 1100K, (f) refs [15-16], (g) refs. [17-19],

To calculate the misorientation stresses, the alumina layers alone were cooled 800 K with free boundary conditions, as in reference [7]. To introduce the effect of the substrate, models including the $\text{TiC}_x\text{N}_{1-x}$ layers (as in Fig. 1) were used. Because the properties for $\text{TiC}_x\text{N}_{1-x}$ are not known, we made the following approximations. Assuming $x = 0.5$, the CTE was taken as the average of the CTEs of TiC and TiN and the components of the stiffness matrix were also assumed to be averages of the components of each phase. In each case, the coatings were supported by a 95 v/o WC and 5 v/o Co substrate. To simulate the shrinking of the substrate, the macroscopic strain was estimated and this was applied as a boundary condition on the left and right hand side of the sample [9]. To specify this boundary condition, we used the CTEs of WC and Co to estimate a composite CTE ($6.6 \times 10^{-6}/\text{K}$) and then assumed a -800 K change in temperature. The resulting strain is -0.0053 and half of this amount was applied to the left and right hand sides of the model. With these conditions, the stress and strain were calculated at each point within the microstructure. In one case (for sample 1), an EBSD map of the substrate (see Fig. 2) was added below the $\text{TiC}_x\text{N}_{1-x}$ layer for comparison. For this case, the properties of WC and Co listed in Table I were assigned for the calculation. It should be noted that the EBSD map in Fig. 2 was obtained near the substrate coating interface, a region that is enriched in Co with respect to the bulk composition. The Co points were not indexed, so this was treated as an isotropic phase. In earlier studies of bulk cemented carbides, this approach was shown to lead to acceptable results [20-21].

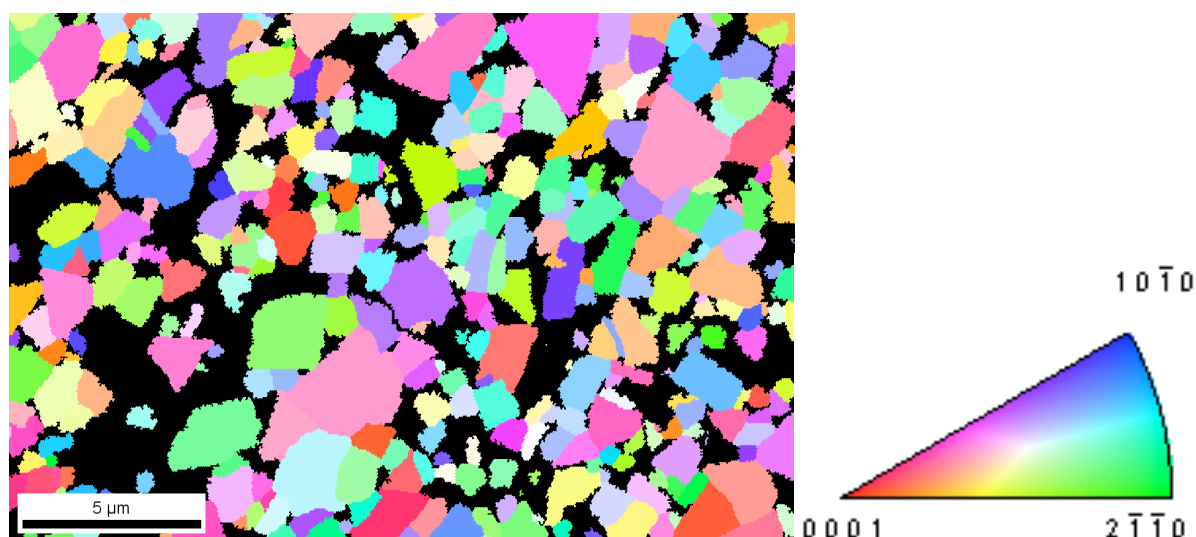


Fig. 2: Inverse pole figure map of the WC/Co substrate of sample 1. Different colors indicate different grain orientations, according to the legend on the right. Black indicates the Co locations.

Results

Inverse pole figure maps for the $\alpha\text{-Al}_2\text{O}_3$ and $\text{TiC}_x\text{N}_{1-x}$ layers of sample 3 are shown in Fig. 1 and similar images of the other three samples were presented in reference [5]. Note that the growth direction is vertical. The grain colors correspond to the orientations defined in the legend. Inverse pole figures for these data are illustrated in Fig. 3. The grain sizes and shape in sample 3 are similar to those of the other three samples (see Table II). The $\text{TiC}_x\text{N}_{1-x}$ layer in sample 3 has weak (112) texture and is similar to the corresponding layers in samples 1 and 2. The closest low index orientation to the $\alpha\text{-Al}_2\text{O}_3$ growth direction is $(10\bar{1}4)$; the other three samples have basal or near basal orientation. (Note that in samples 1 and 2, the maxima was inclined by 5° from the c-axis, along the approximate $[10\bar{1}4]$ direction. This was erroneously labeled as $\{10\bar{1}4\}$ texture in reference [5]; the plane perpendicular to $[10\bar{1}4]$ should be labeled $\{10\bar{1}31\}$.)

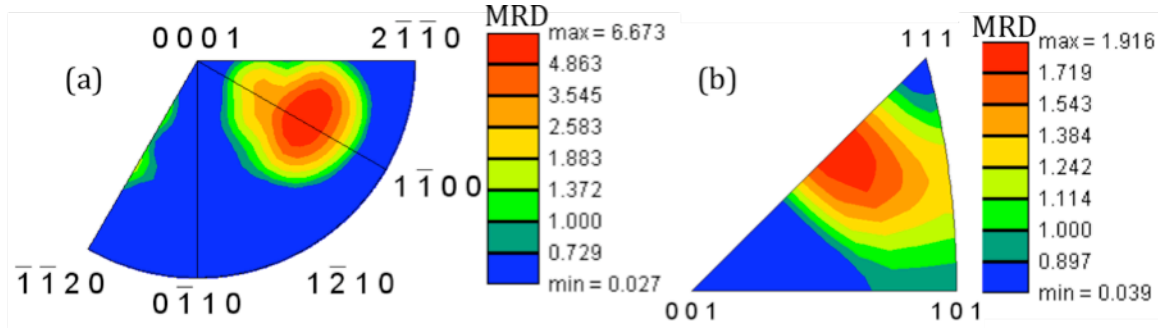


Fig. 3: Inverse pole figures for the growth direction of the (a) α - Al_2O_3 and (b) $\text{TiC}_x\text{N}_{1-x}$ layers of sample 3. The units are multiples of a random distribution.

The microstructural characteristics of the four samples are listed in Table II. Note that two different values for the texture intensity are reported. The global value is determined from all of the data. The local value is determined only from the subset of the microstructure that was used in the finite element simulation. The differences arise because the local value does not sample as many orientations as the global value. While the global value is expected to be a more accurate characterization of the sample, it is more meaningful to consider the local values when comparing the calculated thermal stresses from the different samples. Three of the coatings have basal oriented texture of different strengths, and sample 3 has $(10\bar{1}4)$ texture. Similarly, three of the $\text{TiC}_{1-x}\text{N}_x$ layers have a similar (112) texture while the fourth has (110) texture.

Table II: Summary of Microstructural Characteristics of the Coatings

layer	sample	grains	grain area, μm^2	major axis, μm	minor axis, μm	texture	texture strength global, MRD	texture strength local, MRD
$\text{TiC}_{1-x}\text{N}_x$	1	5538	2.1	4.85	0.67	(112)	1.4	1.6
	2	1112	1.6	3.46	0.69	(112)	1.5	1.4
	3	2611	1.13	2.59	0.62	(112)	1.3	1.9
	4	2050	3.34	5.03	0.79	(110)	3.1	3.2
Al_2O_3	1	950	2.05	3.08	0.84	$\sim(0001)$	8.8	9.2
	2	2567	3.9	3.36	1.36	$\sim(0001)$	4.2	7.6
	3	801	1.96	2.60	0.96	$(10\bar{1}4)$	6.7	6.8
	4	568	3.89	4.34	1.07	(0001)	5.2	9.7

The elastically stored strain energy (u , the elastic strain energy per unit volume) is of interest because it influences the amount of work that must be done to initiate brittle failure. The stored energy is calculated in the following way:

$$u = \frac{1}{2} \sum_{i,j} \sigma_{ij} \varepsilon_{ij} \quad (i, j = 1, 2, 3), \quad (1)$$

where σ and ε are the stress and strain, respectively. It is assumed that the regions with the highest stored elastic energy are the most likely failure sites. Plots of the stored elastic energy in alumina are

shown in Fig. 4. These maps provide visual comparison of the results while the histograms in Fig. 5 provide a more quantitative description of the elastic energy and stresses in the material. The visual impression from Fig. 4 is that samples 1 and 4 have more elements with low elastic energy than samples 2 and 3 and fewer elements with high elastic energy. This is verified by the histogram in Fig. 5(a). The stresses in these samples (shown in Fig. 5(b)) are both tensile and compressive and mostly lie in the range of ± 100 MPa. Note that the distribution of thermal stresses in samples 1 and 4 is narrower than in samples 2 and 3.

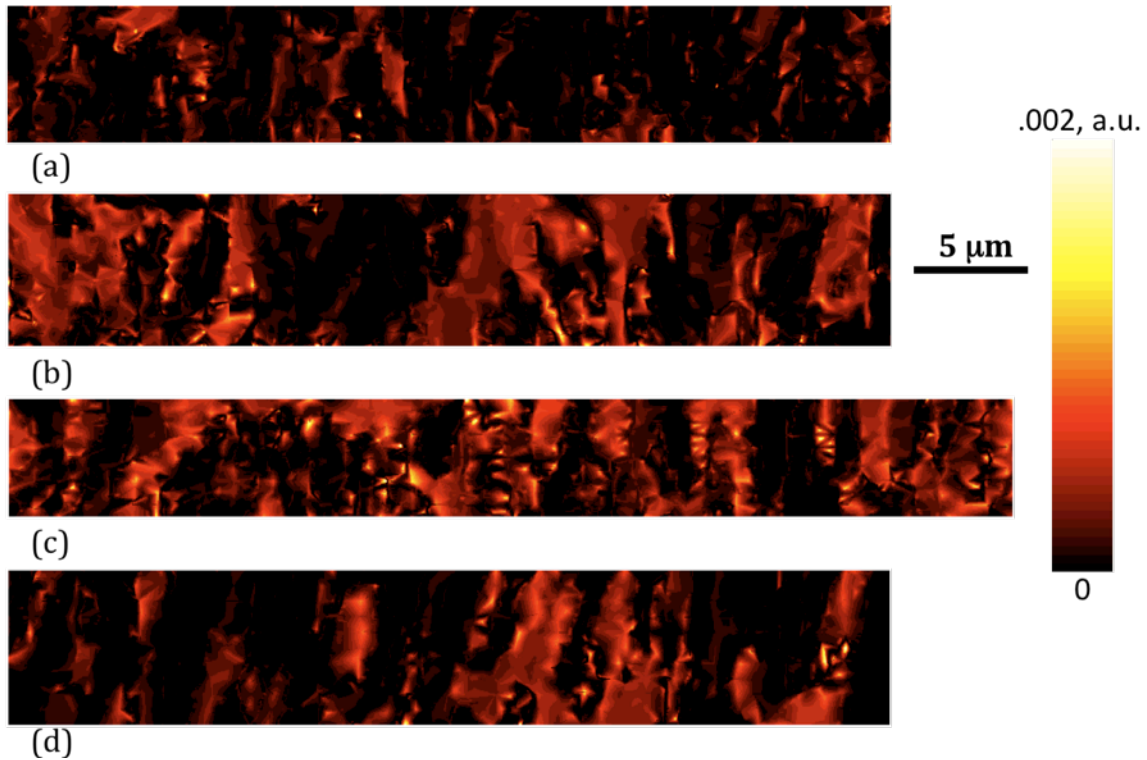


Fig. 4: The stored elastic energy distributions for the four alumina layers computed for $\Delta T = -800$ K and free boundary conditions. The intensity (relative) is indicated by the shading of the figure. (a), (b), (c), and (d) are for sample 1, 2, 3, and 4, respectively.

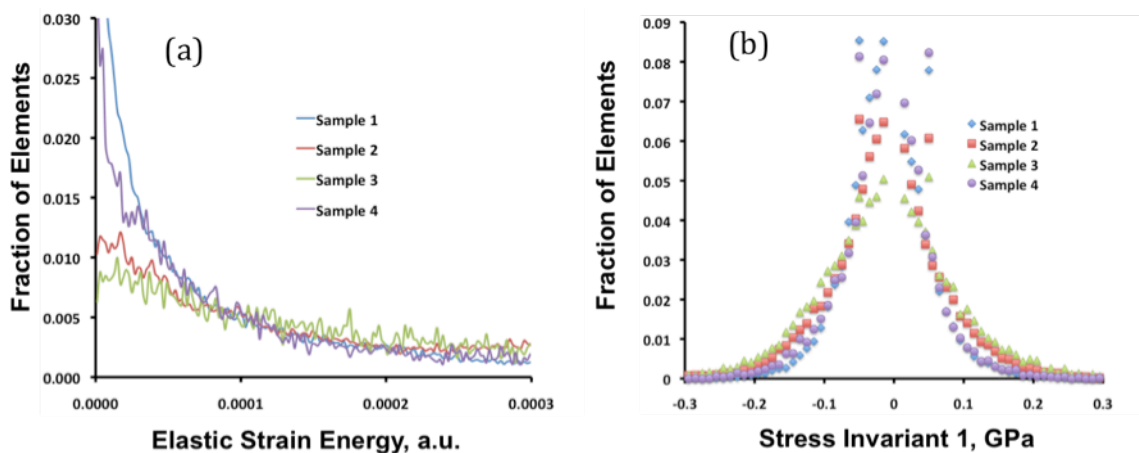


Fig. 5: (a) Histogram of the values of the elastic energy in each element for the four alumina layers computed with free boundary conditions and $\Delta T = -800$ K. (b) Histogram of the values of the stress invariant 1 (trace of the stress tensor) in each element.

The stored elastic energy distributions in the four coatings (with strained lateral boundaries to simulate the shrinking of the substrate) are shown in Fig. 6. The images show that there is broader range of stored elastic energy in the alumina layer and that the elastic energy varies with the sample microstructure. For sample 1, a second simulation was run using a third layer derived from the EBSD map of the composite substrate (see Fig. 2) that was attached below the $\text{TiC}_x\text{N}_{1-x}$ layer. Identical boundary conditions were imposed on the three-layer structure. The stored elastic energy in the alumina was nearly identical in both cases, as illustrated in Fig. 7. Based on this comparison, it was decided that the boundary conditions were sufficient to simulate the influence of the strain imposed by the substrate.

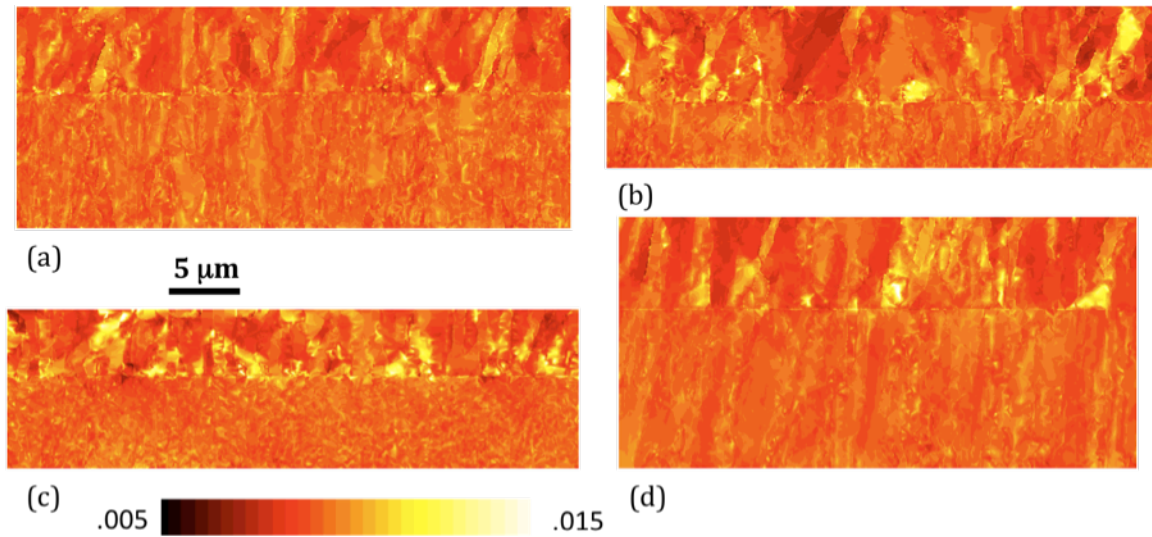


Fig. 6: The stored elastic energy distributions for the coatings computed for $\Delta T = -800$ K and strained lateral boundary conditions. The intensity (relative) is indicated by the shading of the figure. (a), (b), (c), and (d) are for sample 1, 2, 3, and 4, respectively.

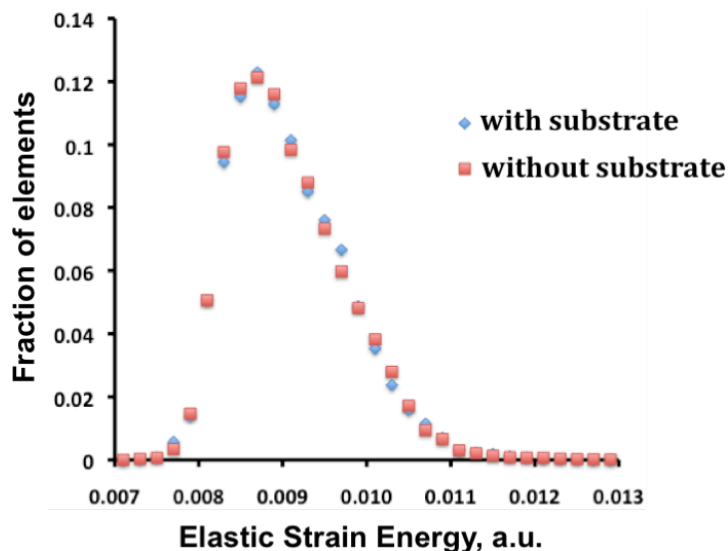


Fig. 7: The elastic energy distributions for sample 1, calculated with and without the WC/Co substrate.

The main component of the strain in the coatings is in the lateral direction, ϵ_{xx} . This is the component of the strain imposed by the substrate and is tensile. The spatial distribution of strains in the coatings is illustrated in Fig. 8. The strains are all tensile. From these images, it is clear that the largest of the tensile strains is in the alumina layer. Furthermore, the distribution of strains in the alumina layers is

much wider than in the $\text{TiC}_x\text{N}_{1-x}$ layers and the width of the distribution varies in the different coatings. The distributions of strains and elastic energy densities are quantified through the histograms in Fig. 9. The strain in the direction parallel to the substrate (ϵ_{xx}) in samples 1 and 4 clearly has a lower average than samples 2 and 3. This same trend is reflected in the values of the stored elastic energy (Fig. 9(b)). The extreme (maximum) values for samples 2 and 3 exceed those of samples 1 and 4.

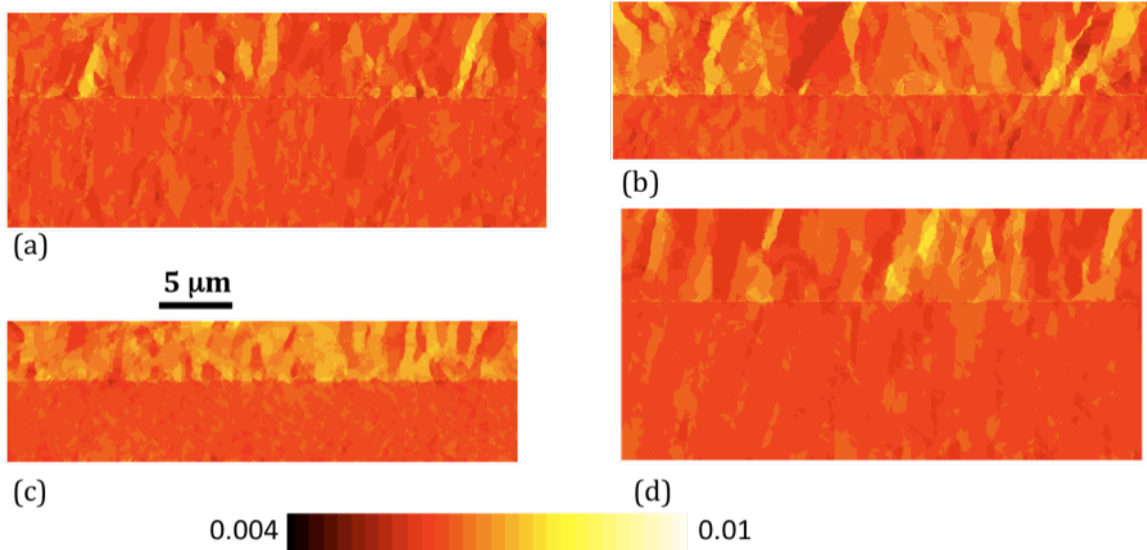


Fig. 8: The horizontal component of the strain (ϵ_{xx}) for the four samples. The magnitude of the strain is indicated by the color. (a), (b), (c), and (d) are for sample 1, 2, 3, and 4, respectively.

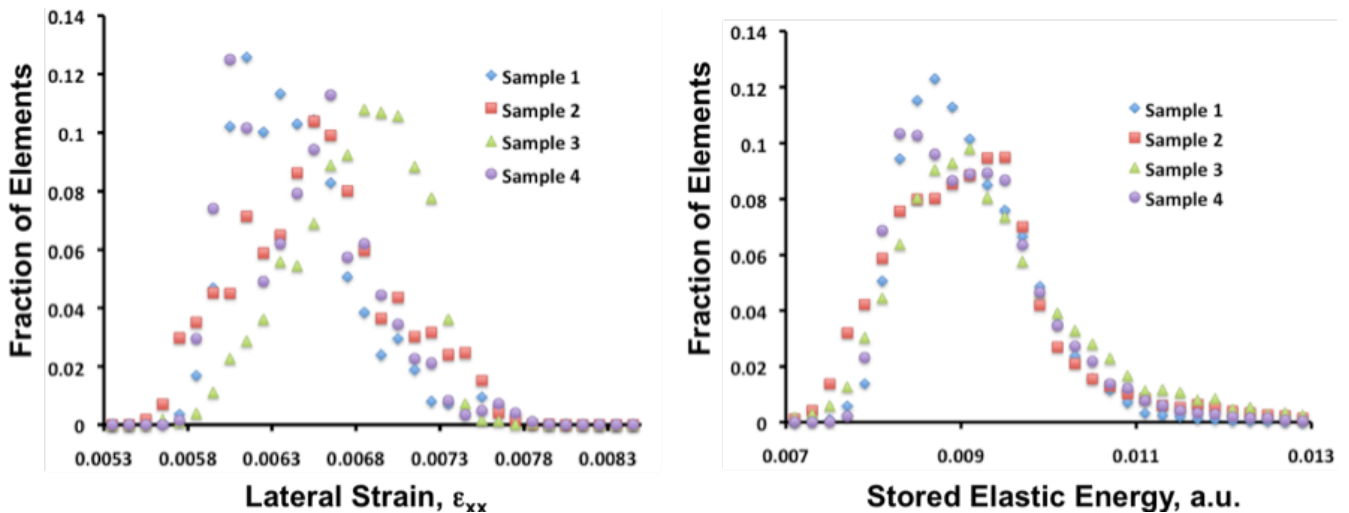


Fig. 9: (a) Histogram of the horizontal component of the strain (ϵ_{xx}) for the four samples, based on the data in Fig. 8. (b) Histogram of the stored elastic energy of the four samples, based on the data in Fig. 7.

Discussion

To begin, we note that the real coatings contain cracks that partially relieve thermal stresses while the structural models used here do not contain any cracks. Therefore, the computed stresses (2 to 3 GPa) exceed those in the real coatings (about 0.5 GPa). Therefore, the results provide us with information

about the pre-cracked state. While it is possible to include cracks in the models, this is beyond the scope of the current work.

It is believed that the extreme values of stored elastic energy are the most important because these are potential fracture initiations sites [7, 20-22]. The maximum values occur consistently in the α -Al₂O₃ layer as opposed to the TiC_xN_{1-x} layer, and for this reason it is concluded that the microstructure of the alumina layer is more important than the TiC_xN_{1-x} layer. The larger variations in the stored elastic energy in α -Al₂O₃ occur because it is trigonal, while TiC_xN_{1-x} is cubic. For this reason, the texture of the α -Al₂O₃ layer is important in determining the residual thermal stresses.

The calculations demonstrate that texture has two important and potentially beneficial impacts on the thermal stresses. First, because alumina has uniaxial symmetry, the alignment of the [0001] axes reduces the misorientation stresses. This is illustrated in Figs. 4 and 5. The samples with the strongest (0001) texture (1 and 4) have a narrower distribution of misorientation stresses than samples 2 and 3. Furthermore, sample 3, with (10 $\bar{1}$ 4) texture, has the highest stresses. While the strength of the texture is about the same as sample 2, the texture does not promote alignment of the unique [0001] axis and, as a result, is not as effective in reducing the misorientation stresses.

When the alumina layers are constrained to be attached to the substrate, these same trends persist. In this case, the local misorientation stresses are compounded by the macroscopic strain associated with the substrate. Once again, we see that the strain and elastic energy density is lower for coatings with more intense (0001) texture. In this case, the anisotropic thermal expansion anisotropy is the source of the reduced strain and stored energy. Alumina contracts more in the [0001] direction than any of the perpendicular directions. Therefore, the best match to the substrate can be obtained by orienting the low CTE directions parallel to the substrate and the high CTE direction perpendicular to the substrate so that the larger dimensional change occurs perpendicular to the free boundaries. Based on these calculations, strong (0001) texture acts to reduce thermal stresses resulting from both local misorientation and conformation to the substrate. In at least one case, coatings with this texture have been observed to have improved resistance to wear during cutting [4]. However, because there are many factors that affect wear processes during cutting, and the relative role of residual stress is not clear, it is not currently possible to directly relate the texture to coating performance.

One noteworthy feature of the stored elastic energy distributions is that maxima are always connected to pairs of grains in which there is a large misalignment of the [0001] axes. It is these extreme points, rather than the mean values, that influence crack formation. Because we are interested in the tails of the distribution, it is reasonable to ask if the amount of material we are considering is a truly representative volume element. With this respect to the texture, the answer is no. This conclusion is based on the differences in the local and global textures (see Table II). However, with respect to extreme values of the stored energy, the size of the simulation volume is probably sufficient. It is known that the crack spacing in these coating is on the order of 50 microns and this is similar to the lateral size of our simulation.

Conclusions

The thermal strains and stored elastic energy in the α -Al₂O₃ layer of coatings on cemented carbide tools are larger than in the TiC_xN_{1-x} layer. The mean value and distribution of stored elastic energy is influenced by the texture in the alumina layer. Increased (0001) texture leads to narrower distributions of stored elastic energy and the lateral thermal strain. Because the distributions are narrower, (0001) textured coatings have fewer extreme values of the stored elastic energy. The results can be explained by the differential thermal expansions in the *a* and *c* directions. The thermal expansion perpendicular to [0001] is less than the thermal expansion parallel to [0001] and, therefore, the thermal expansion mismatch between the alumina coating and the substrate is minimized when grains are oriented with [0001] perpendicular to the substrate.

Acknowledgements

This work was supported primarily by Kennametal Inc. and the Pennsylvania DCED. Partial support by the MRSEC program of the National Science Foundation under Award Number DMR-0520425 is also acknowledged.

References

1. H.G. Prengel, W.R. Prengel, and A.T. Santhanam, *Surf. Coat. Tech.* **102** [3], 183-190, (1998)
2. S. Ruppi, *Int. J. Refract. Met. H.* **23** [4-6], 306-316, (2005)
3. S. Ruppi, A. Larsson, A. Flink, *Thin Solid Films* **516** [18], 5959-5966, (2008)
4. S. Ruppi, *Surf. Coat. Tech.* **202** [17], 4257-4269, (2008)
5. H. Chien, M.C. Gao, H.M. Miller, G.S. Rohrer, Z. Ban, P. Prichard, Y. Liu, *Int. J. Refract. Met. H.* **27** [2], 458-464, (2009)
6. Q. Ma and D.R. Clarke, *J. Am. Ceram. Soc.* **77** [2], 298-302, (1994)
7. V.R. Vedula, S.J. Glass, D.M. Saylor, G.S. Rohrer, W.C. Carter, S.A. Langer, E.R. Fuller, Jr., *J. Am. Ceram. Soc.* **84** [12], 2947-2954, (2001)
8. S.A. Langer, A.C.E. Reid, S.-I. Haan, R.E. García, R.C. Lua, V.R. Coffman, The OOF2 Manual. version 3.7. National Institute of Standards and Technology (NIST); 2007, available online at <http://www.ctcms.nist.gov/oof>
9. C.-H. Hsueh, J.A. Haynes, M.J. Lance, P.F. Becher, M.K. Ferber, E.R. Fuller, Jr., S.A. Langer, W.C. Carter, and W.R. Cannon, *J. Am. Ceram. Soc.* **82** [4], 1073-75, (1999)
10. R.O.E. Vijgen and J.H. Dautzenberg, *Thin Solid Films* **270** [1-2], 264-269, (1995)
11. J.O. Kim, J.D. Achenbach, P.B. Mirkarimi, M. Shinn, and S.A. Barnett, *J. Appl. Phys.* **72** [5], 1805-1811, (1992)
12. W.D. Kingery, H.K. Bowen, D.R. Uhlmann, *Introduction to Ceramics*, 2nd Ed., p. 595, John Wiley and Sons, New York, (1976)
13. D. Maouche, L. Louail, P. Ruterana, M. Maamach, *Comp. Mater. Sci.* **44** [2], 347-350, (2008)
14. J.B. Wachtman, Jr., T.G. Scuderi, and G.W. Creek, *J. Am. Ceram. Soc.* **45** [7], 319-323, (1962)
15. J.R. Gladden, J.H. So, J.D. Maynard, P.W. Saxe, and Y. Le Page, *Appl. Phys. Lett.* **85** [3], 392-395, (2004)
16. D.B. Hovis, A. Reddy, and A.H. Heuer, *Appl. Phys. Lett.* **88** [13], 131910, (2006)
17. M. Lee, R.S. Gilmore, *J Mater. Sci.* **17** [9], 2657-60, (1982)
18. A. Kelly, G.W. Groves, *Crystallography and Crystal Defects*, pp. N, Longman, London, (1973)
19. W.M. Stoll, A.T. Santhanam, *Kirk-Othmer Encyclopedia of Chemical Technology*. 4th ed, John Wiley and Sons, p. 861, (1992)
20. C.-S. Kim, T.R. Massa, and G.S. Rohrer, *Int. J. Ref. Metals. Hard. Mater.*, **24** [1-2], 89-100, (2006)
21. C.-S. Kim, T.R. Massa, and G.S. Rohrer, *J. Am. Ceram. Soc.*, **90** [1], 199-204, (2007)

22. G. Galal Yousef, J. Rödel, E.R. Fuller Jr., A. Zimmerman, B.S. El-Dasher, *J. Am. Ceram. Soc.*, **88** [10], 2809-16, (2005)